SIAM J. SCI. COMPUT.
Vol. 42, No. 2, pp. A1028–A1051

AN EFFICIENT THIRD-ORDER WENO SCHEME WITH UNCONDITIONALLY OPTIMAL ACCURACY*

ANTONIO BAEZA†, RAIMUND BÜRGER‡, PEP MULET†, AND DAVID ZORÍO‡

Abstract. A novel scheme, based on third-order weighted essentially nonoscillatory (WENO) reconstructions, is presented. It attains unconditionally optimal accuracy when the data is smooth enough, even in presence of critical points, and second-order accuracy if a discontinuity crosses the data. The key to attribute these properties to this scheme is the inclusion of an additional node in the data stencil, which is only used in the computation of the weights measuring the smoothness. The accuracy properties of this scheme are proven in detail, and several numerical experiments are presented, which show that this scheme is more efficient in terms of the error reduction versus CPU time than its traditional third-order counterparts as well as several higher-order WENO schemes that are found in the literature.

Key words. third-order WENO reconstructions, optimal accuracy, efficiency

AMS subject classification. 65M06

DOI. 10.1137/19M1260396

1. Introduction.

1.1. Scope. Weighted essentially nonoscillatory (WENO) schemes have become very popular, especially in the context of hyperbolic conservation laws, since they were proposed in [14] and later improved in [12]. One of the most used schemes in the literature is the fifth-order WENO scheme, which in general attains satisfactory results on weak solutions of hyperbolic conservation laws.

Although traditional third-order methods are also widely used, the accuracy loss near smooth extrema is an issue that lowers significantly the accuracy of the numerical solution, even for problems with weak solutions, in which it is significantly smeared.

In this paper we inspect the causes of the misperformance involving the traditional third-order WENO schemes through an analysis of their accuracy near critical points. We propose several solutions to this issue by first proving that it is impossible to prevent accuracy loss near critical points in stencils with only three points, and then showing that it is possible to do so with stencils of at least four points. Ultimately the goal is to present a genuine third-order scheme that is competitive with the most widely used fifth-order schemes for problems with weak solutions.

*Submitted to the journal's Methods and Algorithms for Scientific Computing section May 7, 2019; accepted for publication (in revised form) February 3, 2020; published electronically April 8, 2020.

https://doi.org/10.1137/19M1260396

Funding: The work of the first, third, and fourth authors was supported by Spanish MINECO project MTM2017-83942. The work of the second author was supported by CONICYT/PIA/AFB170001; CRHIAM, project ANID/FONDAP/15130015; Fondecyt project 1170473; and the INRIA Associated Team "Efficient numerical schemes for non-local transport phenomena" (NOLOCO; 2018 2020). The work of the third author was also supported by Conicyt (Chile), project PAI-MEC, folio 80150006. The work of the fourth author was also supported by Conicyt (Chile) through Fondecyt project 3170077.

†Departament de Matemàtiques, Universitat de València, E-46100, Burjassot, Spain (antonio.baeza@uv.es, pep.mulet@uv.es).

‡CI^{2}MA and Departamento de Ingeniería Matemática, Universidad de Concepción, Concepción, Chile (rburger@ing-mat.udec.cl, dzorio@ci2ma.udec.cl).

1.2. Related work. To put this work into the proper perspective, we mention several previous attempts that have been made in order to solve the issue involving the accuracy loss near critical points. For instance, in [23], the authors propose a novel smoothness measure based on introducing an additional exponent in the weight formula proposed in [24] associated to WENO-N3 schemes. However, although this measure solves the issue of the accuracy loss near critical points, the resulting weights depend on the scaling of the data due to the additional exponent. Other works improving this idea have been also done, but the issue of the weights depending on the scaling of the data in the weight design still remains; see, for instance, [8, 9, 25].

Many other works deal with the issue by tuning the parameter ε appearing in the weight design, which was initially conceived to be a small quantity used to avoid divisions by zero near constant data, but that was proven later to be crucial to avoid the accuracy loss near critical points if it was scaled properly; see, for instance, [1]. Some recent works deal with this issue in third-order schemes and limiters, for instance, [17, 18].

In the case of higher accuracy order methods, the issue of the accuracy loss near critical points, without relying on tuning or scaling parameters, has been handled more broadly in the literature by proposing new weight designs, such as the WENO-M [10], WENO-Z [5], and Yamaleev–Carpenter methods [27], obtaining partial solutions to the problem for schemes of arbitrary order. In [4] we proposed a method that completely solves the issue for schemes of order higher than 3. In fact, the present work can be seen as a complement of [4], in which the third-order case, that cannot be fit in the general framework, is separately tackled through a new approach.

We will show in this work that it is not possible to build a third-order reconstruction with a stencil of three points satisfying at once the following properties:

- Detection of discontinuities in the data.
- Detection of critical points in the data.
- Independence of nonlinear weights of the scaling of the data (the issue appearing in [23]).
- Unnecessity of tuning/scaling ε (in contrast to the proposals in, e.g., [1, 18]).

And, once exposed, we will propose a novel third-order WENO (WENO3) reconstruction method satisfying at once the aforementioned properties, by using stencils with an additional point, namely, a stencil containing a total of four points. This does not represent an increase of the stencil used to compute the numerical divergence in a semidiscrete scheme, as proven in section 3.2.

1.3. Outline of the paper. This paper is organized as follows: section 2 starts with some preliminaries and definitions that will be used along the work, presented in subsections 2.1 and 2.2, followed by a motivation in subsection 2.3 in which we prove through a counterexample that a third-order WENO scheme cannot attain the optimal accuracy near critical points if a stencil of only three points is used, but that it is possible to attain the optimal accuracy even near critical points if an additional point is added. The proposed scheme, attaining unconditionally third order, is presented in subsection 2.4. In section 3 the key to use this reconstruction strategy in the context of third-order schemes for hyperbolic conservation laws without increasing the computational domain is shown. Section 4 stands for several validation numerical experiments in which our proposed schemes are compared against the most commonly used fifth-order scheme in terms of efficiency; finally, in section 5 some conclusions are drawn.

2. Optimal third-order scheme.

2.1. Preliminaries.

DEFINITION 2.1. *Assume that* $\alpha \in \mathbb{Z}$. *We write* $f(h) = \mathcal{O}(h^\alpha)$ *to denote that* $\limsup_{h\to 0} |f(h)/h^\alpha| < \infty$, *and* $f(h) = \bar{\mathcal{O}}(h^\alpha)$ *if* $f(h) = \mathcal{O}(h^\alpha)$ *and in addition* $\liminf_{h\to 0} |f(h)/h^\alpha| > 0$.

Since, for positive functions f and g,

$$\limsup_{h\to 0} f(h)g(h) \le \limsup_{h\to 0} f(h) \limsup_{h\to 0} g(h),$$

$$\liminf_{h\to 0} f(h)g(h) \ge \liminf_{h\to 0} f(h) \liminf_{h\to 0} g(h),$$

it follows that $\mathcal{O}(h^\alpha)\mathcal{O}(h^\beta) = \mathcal{O}(h^{\alpha+\beta})$ and $\bar{\mathcal{O}}(h^\alpha)\bar{\mathcal{O}}(h^\beta) = \bar{\mathcal{O}}(h^{\alpha+\beta})$.

2.2. Third-order WENO reconstructions. For the sake of exposition we briefly describe two classical third-order WENO approaches. The first is the third-order WENO method defined by the Jiang–Shu approach [12] (henceforth, JS-WENO3), and the second is the third-order WENO method through the Yamaleev–Carpenter approach [26, 27] (henceforth, YC-WENO3). Since they have many parts in common, we will describe both approaches together while pointing out the key differences when necessary.

The input for both cases is an equally spaced three-point stencil (x_{-1}, x_0, x_1), $x_i - x_{i-1} = h > 0$, $i \in \{0, 1\}$, associated with values (f_{-1}, f_0, f_1), where either $f_i = f(x_i)$ (reconstructions from point values, namely, an interpolation procedure in which the data from the stencil is interpreted as point values of a function, with the reconstruction being a point value of that function) or

$$f_i = \frac{1}{h}\int_{x_{i-1/2}}^{x_{i+1/2}} f(x)\,\mathrm{d}x$$

(reconstructions from cell averages, namely, an interpolation procedure in which the data from the stencil is interpreted as cell averages of a function, with the reconstruction being a point value of that function). Here $x_{i+1/2} = (x_i + x_{i+1})/2$, and $\varepsilon > 0$ is a parameter whose original purpose is to be merely a small positive quantity avoiding divisions by zero. We assume that a right-biased reconstruction is sought, so the output is intended to be an approximation of $f(x_{1/2})$. The smoothness indicators [12] are then defined as follows:

$$I_0 := (f_0 - f_{-1})^2, \quad I_1 := (f_1 - f_0)^2, \tag{2.1}$$

along with the corresponding interpolating polynomials associated to each two-point substencil:

$$p_0(x_{1/2}) = -\frac{1}{2}f_{-1} + \frac{3}{2}f_0, \quad p_1(x_{1/2}) = \frac{1}{2}f_0 + \frac{1}{2}f_1. \tag{2.2}$$

Now, in each case we define

$$\alpha_i = \begin{cases} \dfrac{c_i}{I_i + \varepsilon} & \text{for the JS-WENO3 method,} \\ c_i\left(1 + \dfrac{\sigma}{I_i + \varepsilon}\right) & \text{for the YC-WENO3 method,} \end{cases} \tag{2.3}$$

where $\sigma = (f_1 - 2f_0 + f_{-1})^2$ and

$$(c_0, c_1) = \begin{cases} (1/4, 3/4) & \text{in case of reconstructions from point values,} \\ (1/3, 2/3) & \text{in case of reconstructions from cell averages.} \end{cases} \tag{2.4}$$

Then, the nonlinear weights are computed as

$$\omega_i = \frac{\alpha_i}{\alpha_0 + \alpha_1}, \quad i = 0, 1,$$

and the WENO reconstruction is finally given by

$$p_2(x_{1/2}) = \omega_0 p_0(x_{1/2}) + \omega_1 p_1(x_{1/2}).$$

Remark 2.1. Although the denominator appearing in the expressions of α_i in (2.3) is commonly chosen as $(I_i + \varepsilon)^2$ for third-order schemes, in [1, Note 2] it was proven that, in general, for a $(2r-1)$th-order scheme, a sufficient condition to attain the suboptimal rth-order accuracy when a discontinuity crosses the stencil is using a denominator of the form $(I_i + \varepsilon)^p$ with $2p \geq r$. Therefore, in the particular case of third order ($r = 2$), it suffices to choose $p = 1$, in which theoretical order properties identical to the case $p = 2$ are attained.

2.3. On the accuracy loss of third-order WENO schemes. In the subsequent text we will abuse language by referring to the values of a function on a stencil as the stencil itself.

The following example shows that if a grid $x_{i,h} = z + (c + i)h$, $i \in \{-1, 0, 1\}$, samples a function $f \in \mathcal{C}^2$ such that $f'(z) = 0$ and $f''(z) \neq 0$, then there are cases in which, ignoring the scaling of the stencil $(f_{-1,h}, f_{0,h}, f_{1,h})$, with $f_{i,h} = f(x_{i,h})$, the reconstruction obtained from that stencil for any given h is the same as if the function had a discontinuity in it, and thus there cannot be scaling-independent and dimensionless parameters constructed from the data capable of distinguishing one case from the other.

Let us consider, on one hand, an extreme case by considering $f : \mathbb{R} \to \mathbb{R}$ given by $f(x) = 4x^2$, which satisfies $f'(0) = 0$ and $f''(0) = 8 \neq 0$, and the grid $x_{i,h} = (\frac{1}{2} + i)h$, $i \in \{-1, 0, 1\}$. Then the stencil $F_h = (f_{-1,h}, f_{0,h}, f_{1,h})$, with $f_{i,h} = f(x_{i,h})$, is given by $F_h = (h^2, h^2, 9h^2)$.

On the other hand, we define $g : \mathbb{R} \to \mathbb{R}$ given by $g(x) = 1$ if $x < 0$ and $g(x) = 9$ if $x \geq 0$, with the grid $x_{i,h} = (-\frac{1}{2} + i)h$. Then the stencil $G_h = (g_{-1,h}, g_{0,h}, g_{1,h})$ is given by $G_h = (1, 1, 9)$.

Now, the relationship $F_h = h^2 G_h$ holds for all $h > 0$; that is, both stencils are, for fixed h, a scaled version of the same stencil. Therefore, any procedure to analyze smoothness agnostic about the scaling of the data will fail at distinguishing the first case, consisting of smooth data, from the second one, based on data taken from both sides of a discontinuity. Therefore, such procedure, depending on its construction, will either detect asymptotically both cases as smooth data or will interpret both as discontinuous data, being in both cases wrong (giving either false negatives or false positives). The traditional third-order WENO schemes belong to the latter group, in which the detection of discontinuities is prioritized against the detection of critical points, and thus the latter ones are interpreted incorrectly as discontinuities.

2.4. Unconditionally optimal third-order scheme with an additional node. We next present a novel scheme with essentially nonoscillatory properties which attains unconditionally the optimal order of accuracy.

Let $S := (f_{-1}, f_0, f_1)$ be a stencil from a uniform grid, $f_i = f(x_i)$, $i \in \{-1, 0, 1\}$, $x_i = z + (c + i)h$, $i \in \{-1, 0, 1\}$, and $\bar{S} := S \cup \{f_2\} = (f_{-1}, f_0, f_1, f_2)$ the extended stencil. Let us assume that one wishes to perform a (right-biased with respect to S) reconstruction at $x_{1/2} := (x_0 + x_1)/2$ accounting for discontinuities. Then, both for reconstructions from point values and from cell averages, we define the following items.

We define the corresponding interpolating polynomials associated to the substencils $S_0 = (f_{-1}, f_0)$ and $S_1 = (f_0, f_1)$ evaluated at $x_{1/2}$, which are given by (2.2). Their associated Jiang–Shu smoothness indicators are thus given by (2.1). One of the keys here is to define also an additional smoothness indicator, in which the additional node is used, namely,

$$I_2 := (f_2 - f_1)^2. \tag{2.5}$$

Now, given a small quantity $\varepsilon > 0$, we define the weights

$$\tilde{\omega}_0 := \frac{I_1 + \varepsilon}{I_0 + I_1 + 2\varepsilon}, \quad \tilde{\omega}_1 := \frac{I_0 + \varepsilon}{I_0 + I_1 + 2\varepsilon} = 1 - \tilde{\omega}_0. \tag{2.6}$$

We introduce now the corrector weight, given by

$$\omega = \frac{J}{J + \tau + \varepsilon} \quad \text{with } J = I_0(I_1 + I_2) + (I_0 + I_1)I_2, \tag{2.7}$$

which clearly satisfies $0 \le \omega \le 1$, and τ the product of the square of the undivided difference associated to the extended stencil $\bar{S}$ with the sum of the smoothness indicators:

$$\tau := dI, \quad d := (-f_{-1} + 3f_0 - 3f_1 + f_2)^2, \quad I := I_0 + I_1 + I_2. \tag{2.8}$$

We then define the corrected weights as

$$\omega_0 := \omega c_0 + (1 - \omega)\tilde{\omega}_0, \quad \omega_1 := \omega c_1 + (1 - \omega)\tilde{\omega}_1, \tag{2.9}$$

where c_0 and c_1 are specified in (2.4). Finally, the reconstruction result is given by

$$p(x_{1/2}) = \omega_0 p_0(x_{1/2}) + \omega_1 p_1(x_{1/2}). \tag{2.10}$$

The key to analyze the accuracy of our proposed scheme is to first study the accuracy of the corrector weight ω.

DEFINITION 2.2. *We say that a function f has a critical point of order $k \ge 0$ at x if $f^{(l)}(x) = 0$ for $l = 1, \dots, k$ and $f^{(k+1)}(x) \ne 0$.*

PROPOSITION 2.3. *If f has a critical point at z of order k, $k \in \{0, 1\}$, there holds*

$$\omega = \begin{cases} 1 + \mathcal{O}(h^{4-2k}) + \mathcal{O}(\varepsilon) & \text{if } \bar{S} \text{ is smooth, } f \in \mathcal{C}^3, \\ \mathcal{O}(h^2) + \mathcal{O}(\varepsilon) & \text{if a discontinuity crosses } S. \end{cases}$$

Proof. Clearly, by definition and the fact that $J, \tau \ge 0$, there holds $0 \le \omega \le 1$.

Let us first assume that $\bar{S}$ is smooth with $k \in \{0, 1\}$. Then, according to [3, Lemma 2], if $k = 0$, $I_{2,i} = \bar{\mathcal{O}}(h^2)$, $i \in \{0, 1, 2\}$, and if $k = 1$, then there exists $i_0 \in \{0, 1, 2\}$ such that $I_{2,i_0} = \bar{\mathcal{O}}(h^s)$, for some $s \in \{4, 5, 6, \dots\}$, and $I_{2,i} = \bar{\mathcal{O}}(h^4)$, for $i \in \{0, 1, 2\}$, $i \ne i_0$.

Therefore, combining these properties, we deduce that $I_{2,0} + I_{2,1} = \bar{\mathcal{O}}(h^{2+2k})$ and that $I_{2,1} + I_{2,2} = \bar{\mathcal{O}}(h^{2+2k})$. Moreover, since either $I_{2,0} = \bar{\mathcal{O}}(h^{2+2k})$ or $I_{2,2} = \bar{\mathcal{O}}(h^{2+2k})$, it can be concluded that

$$J = I_{2,0}(I_{2,1} + I_{2,2}) + (I_{2,0} + I_{2,1})I_{2,2} = \bar{\mathcal{O}}(h^{4+4k}) + \mathcal{O}(\varepsilon).$$

On the other hand,

$$d = (-f_{-1} + 3f_0 - 3f_1 + f_2)^2 = \mathcal{O}(h^6) = \mathcal{O}(h^6) + \mathcal{O}(\varepsilon),$$
$$I = I_0 + I_1 + I_2 = \mathcal{O}(h^{2+2k}) = \mathcal{O}(h^{2+2k}) + \mathcal{O}(\varepsilon).$$

Therefore $\tau = \mathcal{O}(h^{8+2k})$. Hence, and since by assumption $J \neq 0$,

$$\omega = \frac{J}{J+\tau+\varepsilon} = \frac{1}{1+\dfrac{\tau}{J}} - \mathcal{O}(\varepsilon) = \frac{1}{1+\dfrac{\mathcal{O}(h^{8+2k})}{\bar{\mathcal{O}}(h^{4+4k})}} - \mathcal{O}(\varepsilon) = \frac{1}{1+\mathcal{O}(h^{4-2k})} - \mathcal{O}(\varepsilon)$$
$$= 1 - \mathcal{O}(h^{4-2k}) - \mathcal{O}(\varepsilon).$$

Finally, let us assume that a discontinuity crosses S. Then there exists $i_0 \in \{0,1\}$ such that $I_{2,i_0} = \bar{\mathcal{O}}(1)$. On the other hand, $I_{2,|1-i_0|} = \bar{\mathcal{O}}(h^{2m_0})$ and $I_{2,2} = \bar{\mathcal{O}}(h^{2m_1})$ for some $1 \leq m_0, m_1 \in \{1,2,3,\dots\}$. Now, by these considerations, we have

$$I_{2,0}(I_{2,1} + I_{2,2}) = \begin{cases} \bar{\mathcal{O}}(h^m) & \text{if } i_0 = 0, \\ \bar{\mathcal{O}}(h^{m_0}) & \text{if } i_0 = 1, \end{cases} \quad (I_{2,0} + I_{2,1})I_{2,2} = \bar{\mathcal{O}}(h^{m_1}),$$

with $m := \max\{m_0, m_1\}$.

Under any of these combinations, we obtain

$$J = I_{2,0}(I_{2,1} + I_{2,2}) + (I_{2,0} + I_{2,1})I_{2,2} = \bar{\mathcal{O}}(h^{2m}).$$

On the other hand, since in this case there holds

$$d = (-f_{-1} + 3f_0 - 3f_1 + f_2)^2 = \bar{\mathcal{O}}(1) = \bar{\mathcal{O}}(1) + \mathcal{O}(\varepsilon),$$
$$I = I_0 + I_1 + I_2 = \bar{\mathcal{O}}(1) = \bar{\mathcal{O}}(1) + \mathcal{O}(\varepsilon),$$

then $\tau = \bar{\mathcal{O}}(1)$ and

$$\omega = \frac{J}{J+\tau+\varepsilon} = \frac{1}{1+\dfrac{\tau}{J}} - \mathcal{O}(\varepsilon) = \frac{1}{1+\dfrac{\bar{\mathcal{O}}(1)^2}{\bar{\mathcal{O}}(h^{2m})}} - \mathcal{O}(\varepsilon) = \frac{1}{1+\dfrac{\bar{\mathcal{O}}(1)}{\bar{\mathcal{O}}(h^{2m})}} - \mathcal{O}(\varepsilon)$$
$$= \frac{1}{1+\bar{\mathcal{O}}(h^{-2m})} - \mathcal{O}(\varepsilon) = \frac{1}{\bar{\mathcal{O}}(h^{-2m})} - \mathcal{O}(\varepsilon) = \bar{\mathcal{O}}(h^{2m}) + \mathcal{O}(\varepsilon) = \mathcal{O}(h^2) + \mathcal{O}(\varepsilon),$$

which completes the proof. ∎

Now, let us focus on the computation of the corrected weights.

PROPOSITION 2.4. *For $i \in \{0,1\}$ there holds*

$$\omega_i = \begin{cases} c_i + \mathcal{O}(h^{4-2k}) + \mathcal{O}(\varepsilon) & \text{if } \bar{S} \text{ contains smooth data}, \\ \mathcal{O}(h^2) + \mathcal{O}(\varepsilon) & \text{if a discontinuity crosses } S_i, \\ \mathcal{O}(1) + \mathcal{O}(\varepsilon) & \text{if a discontinuity crosses } S \text{ but not } S_i. \end{cases}$$

Proof. We first recall that $\omega_i = \omega c_i + (1-\omega)\tilde{\omega}_i$. If $\omega = 1 - \mathcal{O}(h^{m_0}) - \mathcal{O}(\varepsilon)$ for some $m_0 \geq 0$, then

$$\omega_i = \big(1 - \mathcal{O}(h^{m_0}) - \mathcal{O}(\varepsilon)\big)c_i + \big(\mathcal{O}(h^{m_0}) + \mathcal{O}(\varepsilon)\big)\tilde{\omega}_i = c_i + \mathcal{O}(h^{m_0}) + \mathcal{O}(\varepsilon),$$

where we have taken into account that $\tilde{\omega}_i$ is an expression at most $\mathcal{O}(1)$, since in particular $0 \leq \tilde{\omega}_i \leq 1$. Therefore, using Proposition 2.3, we obtain the result.

On the other hand, if ω satisfies $\omega = \mathcal{O}(h^{2m_1}) + \mathcal{O}(\varepsilon)$ for some $m_1 \geq 1$, then

$$\omega_i = \big(\mathcal{O}(h^{2m_1}) + \mathcal{O}(\varepsilon)\big)c_i + \big(1 - \mathcal{O}(h^{2m_1}) - \mathcal{O}(\varepsilon)\big)\tilde{\omega}_i = \tilde{\omega}_i + \mathcal{O}(h^{2m_1}) + \mathcal{O}(\varepsilon).$$

Hence, in this case we must focus on the analysis of the accuracy for ω_i. By Proposition 2.3 we have that $\omega = \mathcal{O}(h^{2m_1})$, $m_1 > 0$, if a discontinuity crosses S.

In such case, there exists $i_0 \in \{0,1\}$ such that $I_{i_0} = \bar{\mathcal{O}}(1)$, whereas $I_{1-i_0} = \mathcal{O}(h^2)$. Therefore, in this case we have

$$\tilde{\omega}_{i_0} = \frac{I_{1-i_0} + \varepsilon}{I_0 + I_1 + 2\varepsilon} = \frac{\mathcal{O}(h^2)}{\bar{\mathcal{O}}(1)} + \mathcal{O}(\varepsilon) = \mathcal{O}(h^2) + \mathcal{O}(\varepsilon),$$

$$\tilde{\omega}_{1-i_0} = \frac{I_{i_0} + \varepsilon}{I_0 + I_1 + 2\varepsilon} = \frac{\bar{\mathcal{O}}(1)}{\bar{\mathcal{O}}(1)} + \mathcal{O}(\varepsilon) = \mathcal{O}(1) + \mathcal{O}(\varepsilon).$$

Therefore, taking into account that $\omega_i = \tilde{\omega}_i + \mathcal{O}(h^{2m_1}) + \mathcal{O}(\varepsilon)$ with $m_1 \geq 1$, we obtain

$$\omega_{i_0} = \mathcal{O}(h^2) + \mathcal{O}(\varepsilon), \quad \omega_{1-i_0} = \mathcal{O}(1) + \mathcal{O}(\varepsilon). \qquad \square$$

THEOREM 2.5. *The reconstruction $p(x_{1/2})$ satisfies*

$$p(x_{1/2}) = \begin{cases} f(x_{1/2}) + \mathcal{O}(h^3) & \text{if } \bar{S} \text{ is smooth,} \\ f(x_{1/2}) + \mathcal{O}(h^2) & \text{if a discontinuity crosses } S. \end{cases}$$

Proof. This is a direct consequence of the application of Proposition 2.4 to the expression (2.10), where we also take into account that for reconstructions both from point values and from cell averages, the ideal weights c_i, $i \in \{0,1\}$, satisfy that $c_0 p_0(x_{1/2}) + c_1 p_1(x_{1/2})$ equals the corresponding third-order reconstruction of the same type at $x_{1/2}$. $\square$

Remark 2.2. The cases in which the order of the critical point is $k \geq 2$ are not covered. This is because with this assumption any reconstruction, regardless of the degree of the corresponding polynomials, will attain an order of at least $k+1 \geq 3$. Therefore, the accuracy will be optimal regardless of the values of the weights ω_i, taking into consideration that they always are a convex combination, namely, $\omega_0, \omega_1 \geq 0$ and $\omega_0 + \omega_1 = 1$.

Summary of the algorithm. Input: $\bar{S} = \{f_{-1}, f_0, f_1, f_2\}$, with $f_i = f(x_i)$ or $f_i = \frac{1}{h}\int_{x_{i-1/2}}^{x_{i+1/2}} f(x)\,\mathrm{d}x$, and $\varepsilon > 0$.

1. Compute the corresponding interpolating polynomials evaluated at $x_{1/2}$, which, both in case of reconstructions from point values and from cell averages, are given by (2.2).
2. Compute the corresponding Jiang–Shu smoothness indicators I_0, I_1, and I_2 (including the one considering the rightmost node) by (2.1) and (2.5).
3. Compute the auxiliary weights $\tilde{\omega}_0$ and $\tilde{\omega}_1$ from (2.6).

4. Define τ by (2.8).
5. Compute the corrector weight ω from (2.7).
6. Compute the corrected weights ω_0 and ω_1 from (2.9).
7. Obtain the optimal WENO (OWENO) reconstruction at $x_{1/2}$:

$$p_2(x_{1/2}) = \omega_0 p_0(x_{1/2}) + \omega_1 p_1(x_{1/2}).$$

Output: $\mathcal{R}(f_{-1}, f_0, f_1, f_2, \varepsilon) := p_2(x_{1/2})$.

Comparison of the algorithm with the YC-WENO3 approach. Let us stress the key differences between the YC-WENO3 method and our proposal. Although at first sight both schemes might look similar, as they include squared divided differences including more than two nodes, the new method is not just an extension of YC-WENO3 including an additional downwind node. This additional node is used in the steps involving formulas (2.5) to (2.9), in a manner so that the problem of order loss at the critical points in the YC-WENO3 scheme is avoided. This accuracy loss is due to the fact that the quotient σ/I_i that appears in (2.3) does not converge to zero as $h \to 0^+$ when the point to which the stencil converges, z, satisfies $f'(z) = 0$ and $f''(z) \neq 0$ (namely, when z is a first-order critical point), since in that case there holds $\sigma = \bar{\mathcal{O}}(h^4)$ and $I_i = \mathcal{O}(h^4)$. According to the results presented above, summarized in Theorem 2.5, we have obtained a third-order WENO reconstruction procedure which, unlike the YC-WENO3 approach, attains the optimal third-order accuracy near critical points. It is important to remark that this is in turn consistent with the conclusion obtained in section 2.3, in which it is proven that there cannot exist a three-point interpolator accounting for discontinuities, while in turn maintaining the optimal third-order accuracy near critical points, unless an artificially scaled tuning parameter is used.

3. WENO schemes for systems of conservation laws. In this section we discuss the incorporation of the novel third-order WENO approach in the context of hyperbolic conservation laws. The purpose is to prove that the resulting scheme depends on the same grid points as a standard third-order WENO reconstruction based on a three-point stencil.

3.1. Hyperbolic systems of conservation laws. We will briefly describe in this section the equations and their discretization procedure. We consider hyperbolic systems of ν scalar conservation laws in d space dimensions:

$$\boldsymbol{u}_t + \sum_{i=1}^{d} \boldsymbol{f}^i(\boldsymbol{u})_{x_i} = \boldsymbol{0}, \quad (\boldsymbol{x}, t) \in \Omega \times \mathbb{R}^+ \subseteq \mathbb{R}^d \times \mathbb{R}^+, \quad \boldsymbol{x} = (x_1, \ldots, x_d), \tag{3.1}$$

where $\boldsymbol{u} = \boldsymbol{u}(\boldsymbol{x}, t) \in \mathbb{R}^\nu$ is the sought solution, $\boldsymbol{f}^i : \mathbb{R}^\nu \to \mathbb{R}^\nu$ are given flux density vectors, and

$$\boldsymbol{u} = \begin{pmatrix} u_1 \\ \vdots \\ u_\nu \end{pmatrix}, \quad \boldsymbol{f}^i = \begin{pmatrix} f_1^i \\ \vdots \\ f_\nu^i \end{pmatrix}, \quad i = 1, \ldots, d; \quad \boldsymbol{f} = \begin{bmatrix} \boldsymbol{f}^1 & \cdots & \boldsymbol{f}^d \end{bmatrix}.$$

System (3.1) is complemented with the initial condition

$$u(\boldsymbol{x}, 0) = \boldsymbol{u}_0(\boldsymbol{x}), \quad \boldsymbol{x} \in \Omega,$$

and prescribed boundary conditions.

To describe the spatial discretization, we introduce a Cartesian grid $\mathcal{G}$ formed by points (cell centers) $\boldsymbol{x} = \boldsymbol{x}_{j_1,\dots,j_d} = ((j_1 - \frac{1}{2})h, \dots, (j_d - \frac{1}{2})h) \in \mathcal{G}$ for $h > 0$. In what follows, we use the index vector $\boldsymbol{j} = (j_1, \dots, j_d)$, let $\boldsymbol{e}_i$ denote the ith d-dimensional unit vector, and assume that J is the set of all indices $\boldsymbol{j}$ for which point values of the solution are to be computed. We then advance a semidiscrete scheme in which spatial derivatives are discretized first. The result is a system of ODEs whose numerical solution is iteratively updated in time. To do so, we first define

$$\boldsymbol{U}(t) := \big(\boldsymbol{u}(\boldsymbol{x}_{\boldsymbol{j}}, t)\big)_{\boldsymbol{j}\in J}.$$

To solve (3.1) we utilize the Shu–Osher finite difference scheme [20, 21] with upwind spatial reconstructions of the flux function that are incorporated into numerical flux vectors $\hat{\boldsymbol{f}}^i$ through a Donat–Marquina flux splitting [6]. Thus, the contribution to the flux divergence in the coordinate x_i at point $\boldsymbol{x} = \boldsymbol{x}_{\boldsymbol{j}}$ is given by

$$\boldsymbol{f}^i(\boldsymbol{U})_{x_i}(\boldsymbol{x}_{\boldsymbol{j}}, t) \approx \frac{1}{h}\Big(\hat{\boldsymbol{f}}^i_{\boldsymbol{j}+\frac{1}{2}\boldsymbol{e}_i}\big(\boldsymbol{U}(t)\big) - \hat{\boldsymbol{f}}^i_{\boldsymbol{j}-\frac{1}{2}\boldsymbol{e}_i}\big(\boldsymbol{U}(t)\big)\Big).$$

Then, WENO reconstructions [12] of order $2r+1$ are considered, with special emphasis on the case we are interested in, namely, $r = 1$ (order 3). To specify the time discretization, we write the semidiscrete scheme compactly as

$$\frac{\mathrm{d}}{\mathrm{d}t}\boldsymbol{U}(t) = \boldsymbol{\mathcal{L}}(\boldsymbol{U}(t)), \quad \boldsymbol{\mathcal{L}}\big(\boldsymbol{U}(t)\big) = \big(\mathcal{L}_{\boldsymbol{j}}(\boldsymbol{U}(t))\big)_{\boldsymbol{j}\in J},$$

where we define

$$\mathcal{L}_{\boldsymbol{j}}(\boldsymbol{U}(t)) := \frac{1}{h}\sum_{i=1}^{d}\Big(\hat{\boldsymbol{f}}^i_{\boldsymbol{j}+\frac{1}{2}\boldsymbol{e}_i}\big(\boldsymbol{U}(t)\big) - \hat{\boldsymbol{f}}^i_{\boldsymbol{j}-\frac{1}{2}\boldsymbol{e}_i}\big(\boldsymbol{U}(t)\big)\Big)$$

(with suitable modifications for boundary points).

For the time discretization, we use either the third-order TVD Runge–Kutta scheme proposed in [21] or the approximate Lax–Wendroff approach proposed in [28], which in turn is based on the original Lax–Wendroff approach proposed by Qiu and Shu in [16]. The choice for the time discretization will be specified in each numerical experiment.

3.2. Third-order WENO scheme. Although it may seem that the overall scheme for finite dimensional conservation laws uses more points than the corresponding scheme for classical WENO3 reconstructions, it is not the case, as we now show.

The semidiscrete scheme for a scalar one-dimensional law is

$$u_i'(t) = -\frac{1}{h}\big(\hat{f}_{i+1/2} - \hat{f}_{i-1/2}\big), \tag{3.2}$$

$$\hat{f}_{i+1/2} = \hat{f}(u_{i-1}, u_i, u_{i+1}, u_{i+2}), \tag{3.3}$$

so that the right-hand side of (3.2) depends on approximations $u_j(t) \approx u(x_j, t)$ at a five-point stencil $j = i-2, \dots, i+2$. An ODE solver, such as the third-order TVD Runge–Kutta scheme proposed in [21], is applied to (3.2) to obtain the final time-space accurate scheme.

If the reconstruction (3.3) associated with the cell interface $x_{i+1/2}$ is sought and we define the interval $I(a, b) := [\min\{a, b\}, \max\{a, b\}]$, then we determine for $j \in \{i-1, i, i+1, i+2\}$ the quantities

$$f_j^{i+1/2,+} := \begin{cases} f(u_j) & \text{if } f'(u) > 0 \text{ for all } u \in I(u_i, u_{i+1}), \\ 0 & \text{if } f'(u) < 0 \text{ for all } u \in I(u_i, u_{i+1}), \\ f(u_j) + \alpha_{i+1/2} u_j & \text{otherwise,} \end{cases}$$

$$f_j^{i+1/2,-} := \begin{cases} 0 & \text{if } f'(u) > 0 \text{ for all } u \in I(u_i, u_{i+1}), \\ f(u_j) & \text{if } f'(u) < 0 \text{ for all } u \in I(u_i, u_{i+1}), \\ f(u_j) - \alpha_{i+1/2} u_j & \text{otherwise,} \end{cases}$$

where

$$\alpha_{i+1/2} := \max_{u \in I(u_i, u_{i+1})} \bigl|f'(u)\bigr|.$$

The precise formulation (see [21]) for attaining third-order accuracy (the maximum for semidiscrete stability being three for this five-point stencil; cf. [2]) for the usual WENO3 reconstructions consists in using a local flux splitting $f(u) = f^+(u) + f^-(u)$ such that $\pm(f^{\pm}(u))' \geq 0$, in the interval $I(u_i, u_{i+1}]$ determined by u_i and u_{i+1}, which is defined as

$$\begin{aligned} \hat{f}_{i+1/2} := {} & \mathcal{R}^+\bigl(f_{i-1}^{i+1/2,+}, f_i^{i+1/2,+}, f_{i+1}^{i,+1/2,+}\bigr) \\ & + \mathcal{R}^-\bigl(f_i^{i+1/2,-}, f_{i+1}^{i+1/2,-}, f_{i+2}^{i+1/2,-}\bigr), \end{aligned} \tag{3.4}$$

where $\mathcal{R}^+$ is a right-biased cell-averages reconstruction and is the right-biased cell-averages reconstruction given by $\mathcal{R}^-(a,b,c) = \mathcal{R}^+(c,b,a)$. In contrast, the flux splitting and reconstruction used herein are defined as follows. Instead of using (3.4), we propose to define the flux value $\hat{f}_{i+1/2}$ by our optimal-order reconstruction $\mathcal{R}^{\pm,\mathrm{opt}}$ that depends on the four-point stencil such that

$$\begin{aligned} \hat{f}_{i+1/2} &= \hat{f}(u_{i-1}, u_i, u_{i+1}, u_{i+2}) \\ &= \mathcal{R}^{+,\mathrm{opt}}\bigl(f_{i-1}^{i+1/2,+}, f_i^{i+1/2,+}, f_{i+1}^{i+1/2,+}, f_{i+2}^{i+1/2,+}\bigr) \\ &\quad + \mathcal{R}^{-,\mathrm{opt}}\bigl(f_{i-1}^{i+1/2,-}, f_i^{i+1/2,-}, f_{i+1}^{i+1/2,-}, f_{i+2}^{i+1/2,-}\bigr). \end{aligned}$$

Systems of conservation laws are dealt by the application of the former scheme to local characteristic fields, obtained by a double linearization [6]. The extension to multidimensional Cartesian grids follows by working dimension by dimension.

It is also important to remark that, as pointed out in [2], the maximum order of accuracy that a stable semidiscrete scheme with a numerical domain of dependence of five points can attain is three. This explains why we are not using the additional fourth node (used only for the smoothness analysis) to increase by a unit the order of the reconstructions. Otherwise, and in this particular case, the reconstructions would be centered; thus our scheme would lose the upwind features and ultimately the stability properties.

4. Numerical experiments.

4.1. Accuracy tests with algebraic problems. We perform some tests in order to verify the accuracy properties of the scheme in presence of critical points. To this end, we use the multiple-precision library MPFR [15] through its C++ wrapper [11], using a precision of 3322 bits ($\approx$ 1000 digits) and taking in all cases $\varepsilon = 10^{-10^6}$.

Let us consider the family of functions $f_k : \mathbb{R} \to \mathbb{R}$, $k \in \{0, 1\}$, given by $f_k(x) = x^{k+1}\mathrm{e}^x$. Then f_k has a smooth extremum at $x = 0$ of order k. In this case the error is given by $E_{k,n} = |P_n(0) - f_k(0)|$, where P_n denotes the corresponding reconstruction at $x_{1/2} = 0$, with the grid $x_i = (i - 1/2)h$, $i \in \{-1, \dots, 1 + s\}$ ($s = 0$ for the traditional JS-WENO and YC-WENO schemes and $s = 1$ for the proposed optimal WENO schemes, in which an additional node is considered), with $h = 1/n$ for $n \in \mathbb{N}$, when pointwise values are taken, namely, $f_{k,i} = f_k(x_i)$ and reconstructions from pointwise values to pointwise values are performed. We also present in the tables the same setup when cell average values are taken instead,

$$f_{k,i} = \int_{x_i - h/2}^{x_i + h/2} f(x)\,\mathrm{d}x,$$

by reconstructing pointwise values from cell average values. In all cases, the tables show the corresponding average orders,
$O_k = \frac{1}{80}\sum_{j=1}^{80} o_{k,j}$, where $o_{k,j} = \log_2(E_{k,n_{j-1}}/E_{k,n_j}))$, with $n_j = 5{\cdot}2^j$, $j \in \{0, \dots, 80\}$.

We consider alternatively the family of functions $g_k : \mathbb{R} \to \mathbb{R}$, $k \in \{0, 1\}$ given by

$$g_k(x) = \begin{cases} x^{2k}\mathrm{e}^x & \text{for } x \le 0, \\ \mathrm{e}^{x+1} & \text{for } x > 0. \end{cases}$$

Then g_k has a discontinuity at $x = 0$ with a left smooth extremum of order k for $k \in \{0, 1\}$. We test the accuracy of the methods with the same parameters as above, where, in order to emphasize the behavior of our optimal scheme at discontinuities, in this case we change the location of the discontinuity by considering a grid of the form $x_i = (i - \frac{1}{2} + \theta)h$, $i \in \{-1, \dots, 1 + s\}$ for $\theta \in \{0, 1\}$. Since $x_{1/2} = \theta h$, the error is thus now given by $|P(\theta h) - g(\theta h)|$.

The results involving the different combinations of the proposed values for k in the case of f_k and for θ and k in the case of g_k are shown in Table 1 for the traditional JS-WENO3 and YC-WENO3 schemes as well as the optimal WENO approach presented herein.

We discuss row by row the results obtained in Table 1. The first two rows containing data stand for the function f_k, which is a smooth function with a critical point of order k. Therefore, the optimal order is 3. We can see that when the critical point has order zero, namely, $k = 0$, all the schemes attain the optimal accuracy. However, differences arise when $k = 1$. In this case, the first-order critical point affects the traditional WENO schemes decreasing its accuracy in one unit, whereas the optimal WENO approach keeps the optimal third-order accuracy.

As for the function g_k, we can conclude that regardless of the position of the discontinuity with respect to the stencil S and the order of the critical point, all the

TABLE 1
Numerical order for third-order schemes, functions with smooth extrema.

	θ	k	JS-WENO3		YC-WENO3		OWENO3	
			Point	Cell	Point	Cell	Point	Cell
f_k	—	0	3.00	3.00	2.98	2.98	3.00	3.00
	—	1	2.00	2.00	2.00	2.00	**3.01**	**3.01**
g_k	0	0	1.97	1.93	1.98	1.98	2.00	2.00
	0	1	1.99	1.99	1.99	1.99	1.96	1.95
	1	0	2.00	2.00	2.00	2.00	1.99	2.00
	1	1	2.00	2.00	2.00	2.00	2.00	2.00

schemes, both the traditional ones and the optimal ones, attain the suboptimal second-order accuracy, avoiding the error of magnitude $\bar{\mathcal{O}}(1)$ associated to the substencil containing the discontinuity. This is the best order of accuracy that can be obtained near a discontinuity by shock-capturing methods based on three- or four-point stencils.

4.2. Conservation law experiments. In this section we present some experiments involving numerical solutions of hyperbolic conservation laws. We discretize them in time by the approximate Lax–Wendroff approach matching the spatial order proposed in [28], unless we indicate the contrary, in which case the third-order TVD Runge–Kutta scheme [21] will be used. Also, since in this case we work with double precision, the ε parameter is chosen as $\varepsilon = 10^{-100}$. The flux splitting used is Donat–Marquina [6] for the problems with weak solutions and local Lax–Friedrichs for the problems with smooth solutions (unless all the characteristics move to the same direction, in whose case we simply use the corresponding left/right-biased upwind reconstructions). In all cases, and also unless we state the contrary, the CFL used for the one-dimensional (1D) experiments is 0.5 and 0.4 for the two-dimensional (2D) experiments. The reason for the choice of these CFL values is for uniformity reasons, combined with the fact that in some problems with complex structures or interactions between discontinuities, the fifth-order WENO method combined with the flux splitting used [6] can develop some oscillations (such as in the double Mach reflection problem, in Example 5) or even fail (such as in the blast wave problem, in Example 4) if larger CFL values are used. It must be pointed out that these issues have not been observed on any of the third-order methods for larger CFL values.

Example 1: Linear advection equation. We consider the linear advection equation with the following domain, boundary condition, and initial condition:

$$u_t + f(u)_x = 0, \quad \Omega = (-1,1), \quad u(-1,t) = u(1,t),$$
$$f(u) = u, \quad u_0(x) = 0.25 + 0.5\sin(\pi x),$$

whose exact solution is $u(x,t) = 0.25 + 0.5\sin(\pi(x-t))$ with critical points located at $x = t + m + 1/2$, $m \in \mathbb{Z}$. We run several simulations with final time $T = 1$, resolutions of n points, that is, with a grid spacing of $h = 2/n$, using the classical JS-WENO schemes, YC-WENO, and our OWENO3 scheme, both with the $\|\cdot\|_1$ and $\|\cdot\|_\infty$ errors. Since the characteristics move to the right, we use left-biased reconstructions. The results are shown in Table 2. From the table it can be appreciated that an accuracy loss is produced in the case of the traditional schemes, whereas the optimal third-order accuracy is solidly kept by the novel scheme.

Examples 2a and 2b: Burgers equation. We now consider the Burgers equation with the following setup involving the domain, boundary conditions, and initial condition:

$$u_t + f(u)_x = 0, \quad \Omega = (-1,1), \quad u(-1,t) = u(1,t),$$
$$f(u) = u^2/2, \quad u_0(x) = 0.25 + 0.5\sin(\pi x). \tag{4.1}$$

In this case, $f(u_0(x))$ has first-order smooth extrema at $x = -1/2$ and at $x = 1/2$. In Example 2a, we consider the solution of (4.1) at $T = 0.3$, when it is still smooth, whose results are shown in Table 3, while in Example 2b we set $T = 12$, when the solution of (4.1) has become discontinuous, shown in Figure 1, in which are also compared against the results obtained by the widely used JS-WENO5 schemes.

From Table 3 one can see that again, as in the linear advection case, the presence of first-order critical points makes the accuracy of the traditional schemes decay to

TABLE 2
Example 1: *Linear advection equation, third-order schemes.*

	JS-WENO3				YC-WENO3				OWENO3			
	$\|\cdot\|_1$		$\|\cdot\|_\infty$		$\|\cdot\|_1$		$\|\cdot\|_\infty$		$\|\cdot\|_1$		$\|\cdot\|_\infty$	
n	Err.	$\mathcal{O}$	Err.	$\mathcal{O}$	Err.	$\mathcal{O}$	Err.	$\mathcal{O}$	Err.	$\mathcal{O}$	Err.	$\mathcal{O}$
40	8.52e-03	—	2.56e-02	—	6.67e-03	—	2.11e-02	—	1.87e-04	—	3.08e-04	—
80	2.10e-03	2.02	1.00e-02	1.36	1.46e-03	2.19	7.90e-03	1.42	2.31e-05	3.02	3.66e-05	3.07
160	4.86e-04	2.11	3.81e-03	1.39	3.19e-04	2.20	2.87e-03	1.46	2.86e-06	3.01	4.50e-06	3.02
320	1.10e-04	2.15	1.43e-03	1.42	6.45e-05	2.31	1.02e-03	1.50	3.56e-07	3.01	5.60e-07	3.01
640	2.45e-05	2.16	5.28e-04	1.43	1.32e-05	2.29	3.54e-04	1.52	4.44e-08	3.00	6.98e-08	3.00
1280	5.42e-06	2.18	1.94e-04	1.45	2.61e-06	2.34	1.21e-04	1.55	5.55e-09	3.00	8.72e-09	3.00
2560	1.19e-06	2.19	7.06e-05	1.46	5.05e-07	2.37	4.10e-05	1.56	6.93e-10	3.00	1.09e-09	3.00
5120	2.57e-07	2.21	2.56e-05	1.46	9.69e-08	2.38	1.37e-05	1.58	8.67e-11	3.00	1.36e-10	3.00
10240	5.54e-08	2.21	9.22e-06	1.47	1.84e-08	2.40	4.53e-06	1.60	1.08e-11	3.00	1.71e-11	2.99
20480	1.19e-08	2.22	3.31e-06	1.48	3.44e-09	2.42	1.49e-06	1.61	1.43e-12	2.92	2.38e-12	2.84

TABLE 3
Example 2a: *Burgers equation, third-order schemes.*

	JS-WENO3				YC-WENO3				OWENO3			
	$\|\cdot\|_1$		$\|\cdot\|_\infty$		$\|\cdot\|_1$		$\|\cdot\|_\infty$		$\|\cdot\|_1$		$\|\cdot\|_\infty$	
n	Err.	$\mathcal{O}$	Err.	$\mathcal{O}$	Err.	$\mathcal{O}$	Err.	$\mathcal{O}$	Err.	$\mathcal{O}$	Err.	$\mathcal{O}$
40	1.77e-03	—	1.11e-02	—	1.62e-03	—	9.85e-03	—	1.70e-04	—	1.11e-03	—
80	4.77e-04	1.89	4.17e-03	1.41	4.21e-04	1.95	3.57e-03	1.46	2.24e-05	2.92	1.81e-04	2.62
160	1.18e-04	2.02	1.62e-03	1.36	9.80e-05	2.10	1.32e-03	1.43	2.75e-06	3.03	2.27e-05	3.00
320	2.91e-05	2.02	6.21e-04	1.38	2.24e-05	2.13	4.94e-04	1.42	3.37e-07	3.03	2.77e-06	3.03
640	7.01e-06	2.06	2.36e-04	1.40	5.05e-06	2.15	1.79e-04	1.46	4.16e-08	3.02	3.41e-07	3.02
1280	1.64e-06	2.10	8.84e-05	1.42	1.11e-06	2.18	6.36e-05	1.50	5.17e-09	3.01	4.23e-08	3.01
2560	3.83e-07	2.10	3.28e-05	1.43	2.47e-07	2.17	2.21e-05	1.52	6.44e-10	3.00	5.26e-09	3.01
5120	8.85e-08	2.11	1.20e-05	1.45	5.45e-08	2.18	8.84e-06	1.32	8.04e-11	3.00	6.56e-10	3.00
10240	2.04e-08	2.11	5.42e-06	1.15	1.21e-08	2.17	4.41e-06	1.00	1.00e-11	3.00	8.19e-11	3.00
20480	4.70e-09	2.12	2.73e-06	0.99	2.71e-09	2.16	2.21e-06	1.00	1.25e-12	3.00	1.02e-11	3.00

orders lower than three, while the third-order accuracy is still kept by the optimal third-order scheme. As for the discontinuous case, we can see in Figure 1 that the optimal third-order scheme has a much higher resolution than the traditional third-order schemes, especially near the discontinuity and, moreover, it is similar to the resolution presented by the fifth-order scheme.

Examples 3a and 3b: Shu–Osher problem. The 1D Euler equations for gas dynamics are given by $\boldsymbol{u} = (\rho, \rho v, E)^{\mathrm{T}}$ and $\boldsymbol{f}(\boldsymbol{u}) = \boldsymbol{f}^1(\boldsymbol{u}) = (\rho v, p + \rho v^2, v(E+p))^{\mathrm{T}}$, where ρ is the density, v is the velocity, E is the specific energy of the system, and p is the pressure, given by the equation of state $p = (\gamma - 1)(E - \rho v^2/2)$, where γ is the adiabatic constant that will be taken as $\gamma = 1.4$. We now consider the interaction with a Mach 3 shock and a sine wave. The spatial domain is now given by $\Omega := (-5, 5)$ with the initial condition

$$(\rho, v, p)(x, 0) = \begin{cases} (27/7, 4\sqrt{35}/9, 31/3) & \text{if } x \le -4, \\ (1 + \sin(5x)/5, 0, 1) & \text{if } x > -4, \end{cases}$$

with left inflow and right outflow boundary conditions.

We run the simulation until $T = 1.8$ and compare the schemes against a reference solution computed with a resolution of $n = 16000$ cells. Figures 2 and 3 are associated to the third-order schemes and JS-WENO5 with resolutions of $n = 200$ and $n = 400$ points, respectively, showing the corresponding density fields.

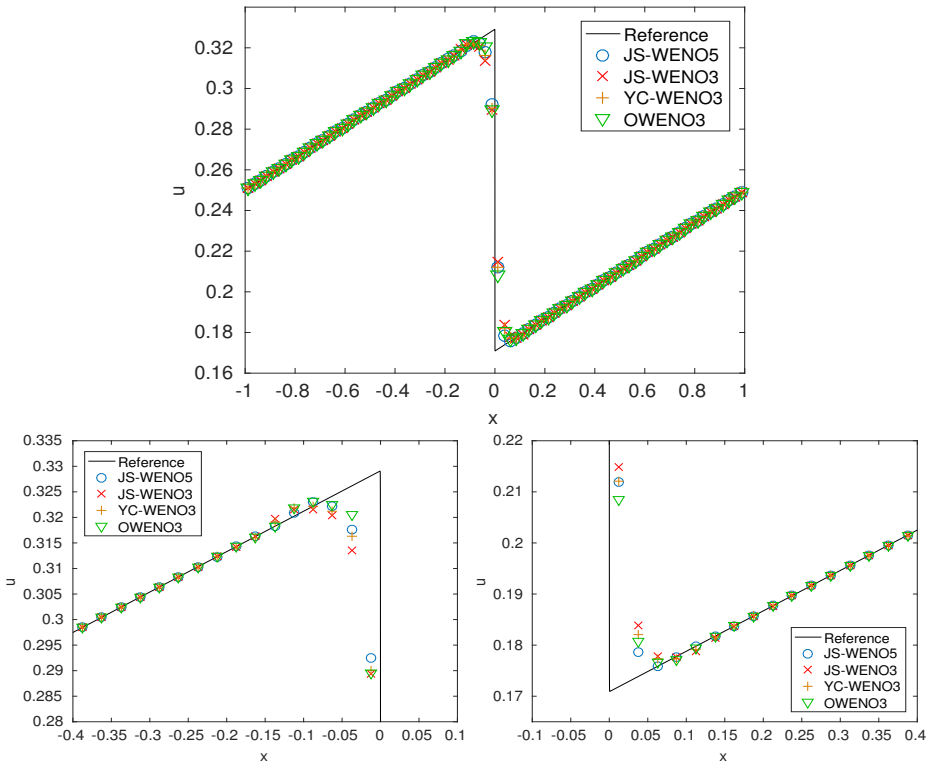

FIG. 1. *Example* 2b *(Burgers equation, discontinuous solution at* $T = 12$*): Third-order schemes.*

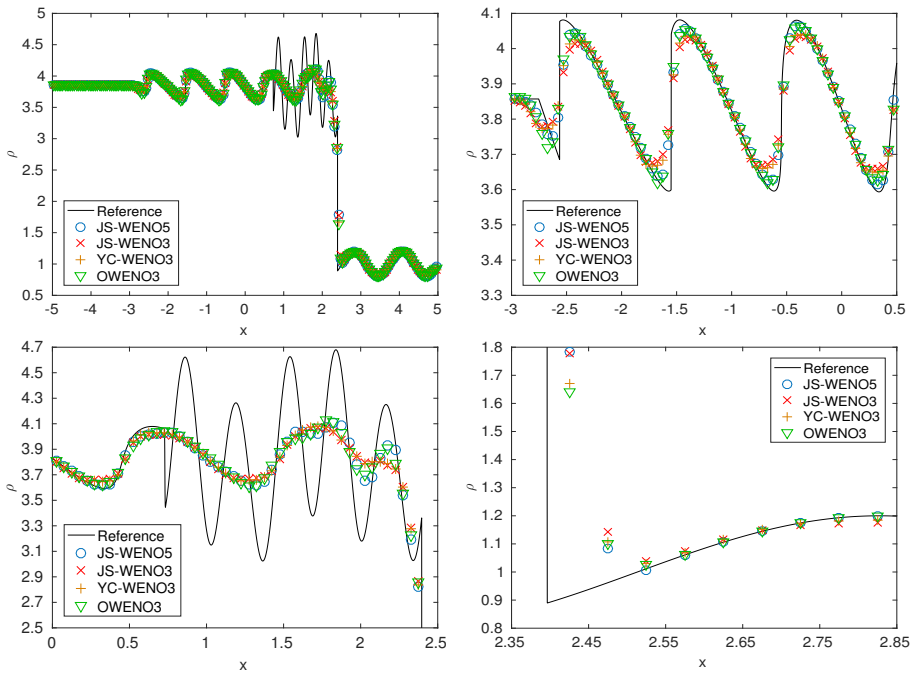

FIG. 2. *Example* 3a: *Shu–Osher problem.* $T = 1.8$. $n = 200$.

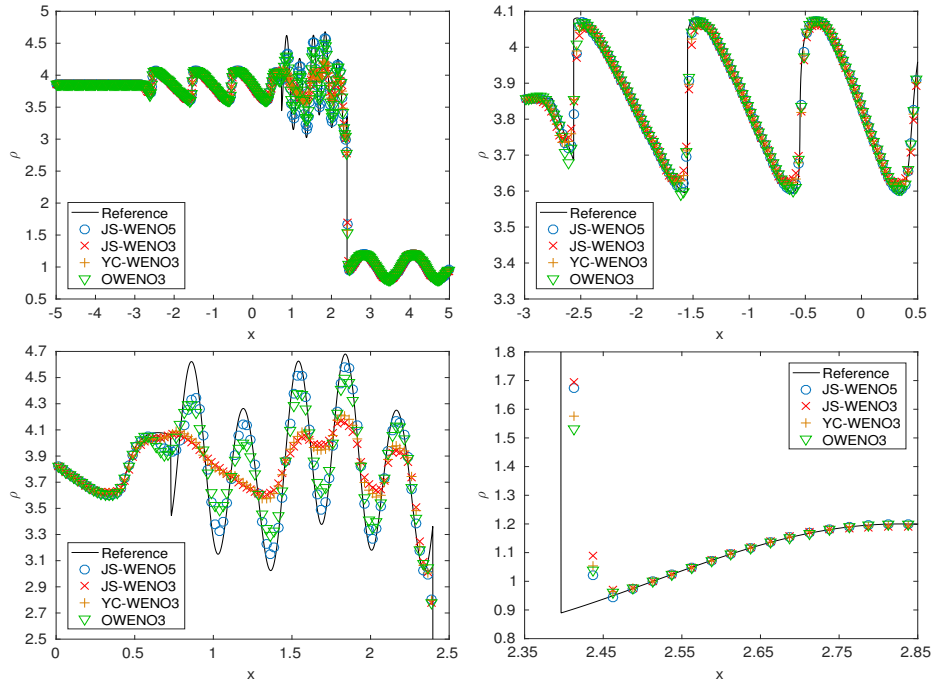

FIG. 3. *Example* 3a: *Shu–Osher problem.* $T = 1.8$. $n = 400$.

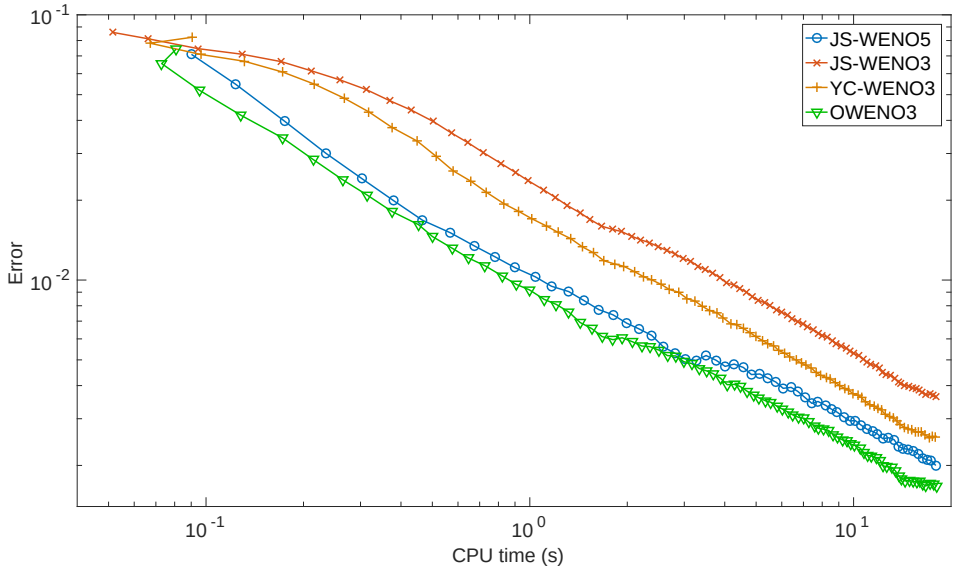

FIG. 4. *Example* 3b: *Ratio error/CPU comparison for Shu–Osher problem.*

The third-order optimal schemes show again a much better resolution than their traditional counterparts, especially observed in the resolution of $n = 400$ cells. Moreover, they have a similar resolution than the JS-WENO5 scheme, and at lower computational cost. In order to support the latter statement, we next present an efficiency comparison involving the ratio error $\|\cdot\|_1$ / CPU time, which can be seen in Figure 4.

The proposed third-order scheme shows a better performance than its traditional counterparts. Moreover, it is also more efficient than the JS-WENO5 scheme in this case.

Examples 4a and 4b: Blast wave problem. Continuing with the 1D Euler equations, let us now simulate the interaction of two blast waves [22] by using the following initial data:

$$u(x,0) = \begin{cases} u_{\mathrm{L}} & \text{if } 0 < x < 0.1, \\ u_{\mathrm{M}} & \text{if } 0.1 < x < 0.9, \\ u_{\mathrm{R}} & \text{if } 0.9 < x < 1, \end{cases}$$

where $\rho_{\mathrm{L}} = \rho_{\mathrm{M}} = \rho_{\mathrm{R}} = 1$, $v_{\mathrm{L}} = v_{\mathrm{M}} = v_{\mathrm{R}} = 0$, $p_{\mathrm{L}} = 10^3, p_{\mathrm{M}} = 10^{-2}, p_{\mathrm{R}} = 10^2$. We set reflecting boundary conditions at $x = 0$ and $x = 1$, simulating a solid wall at both sides. This problem involves multiple reflections of shocks and rarefactions off the walls and many interactions of waves inside the domain.

The results are shown in Figure 5 for the density field at a resolution of $n = 800$ cells, in which all the third-order schemes involved in this paper are used, being in turn compared with the JS-WENO5 scheme. The resolution used for the reference solution is $n = 100000$ cells.

As the results show, the third-order optimal scheme has at some regions a higher resolution than even the fifth-order scheme. Finally, Figure 6 shows an efficiency comparison between all the involved schemes, where, for the sake of performing a fair comparison, all the schemes have been equipped with the third-order TVD Runge–Kutta scheme [21]. In this case, the optimal third-order scheme is still more efficient than the fifth-order scheme.

Examples 5a and 5b: Double Mach reflection. The equations that will be considered in this section are the 2D Euler equations for inviscid gas dynamics given by

$$\boldsymbol{u}_t + \sum_{i=1}^{d} \boldsymbol{f}^i(\boldsymbol{u})_{x_i} = \boldsymbol{0}, \quad (\boldsymbol{x}, t) \in \Omega \times \mathbb{R}^+ \subseteq \mathbb{R}^d \times \mathbb{R}^+, \quad \boldsymbol{x} = (x_1, \ldots, x_d), \tag{4.2}$$

by taking in (4.2) $m = 4$ and $d = 2$, where setting $x = x_1$ and $y = x_2$, we have

$$\boldsymbol{u} = \begin{pmatrix} \rho \\ \rho v^x \\ \rho v^y \\ E \end{pmatrix}, \quad \boldsymbol{f}^1(\boldsymbol{u}) = \begin{pmatrix} \rho v^x \\ p + \rho (v^x)^2 \\ \rho v^x v^y \\ v^x (E + p) \end{pmatrix}, \quad \boldsymbol{f}^2(\boldsymbol{u}) = \begin{pmatrix} \rho v^y \\ \rho v^x v^y \\ p + \rho (v^y)^2 \\ v^y (E + p) \end{pmatrix}.$$

Here ρ is the density, (v^x, v^y) is the velocity, E is the specific energy, and p is the pressure that is given by the equation of state $p = (\gamma - 1)(E - \rho((v^x)^2 + (v^y)^2)/2)$, where the adiabatic constant is again chosen as $\gamma = 1.4$.

This experiment uses these equations to model a vertical rightgoing Mach 10 shock colliding with an equilateral triangle. By symmetry, this is equivalent to a collision with a ramp with a slope of 30° with respect to the horizontal line.

For the sake of simplicity, in [22] the equivalent problem is considered in a rectangle, consisting in a rotated shock, whose vertical angle is 30°. The domain is the rectangle $\Omega = [0, 4] \times [0, 1]$, and the initial conditions are

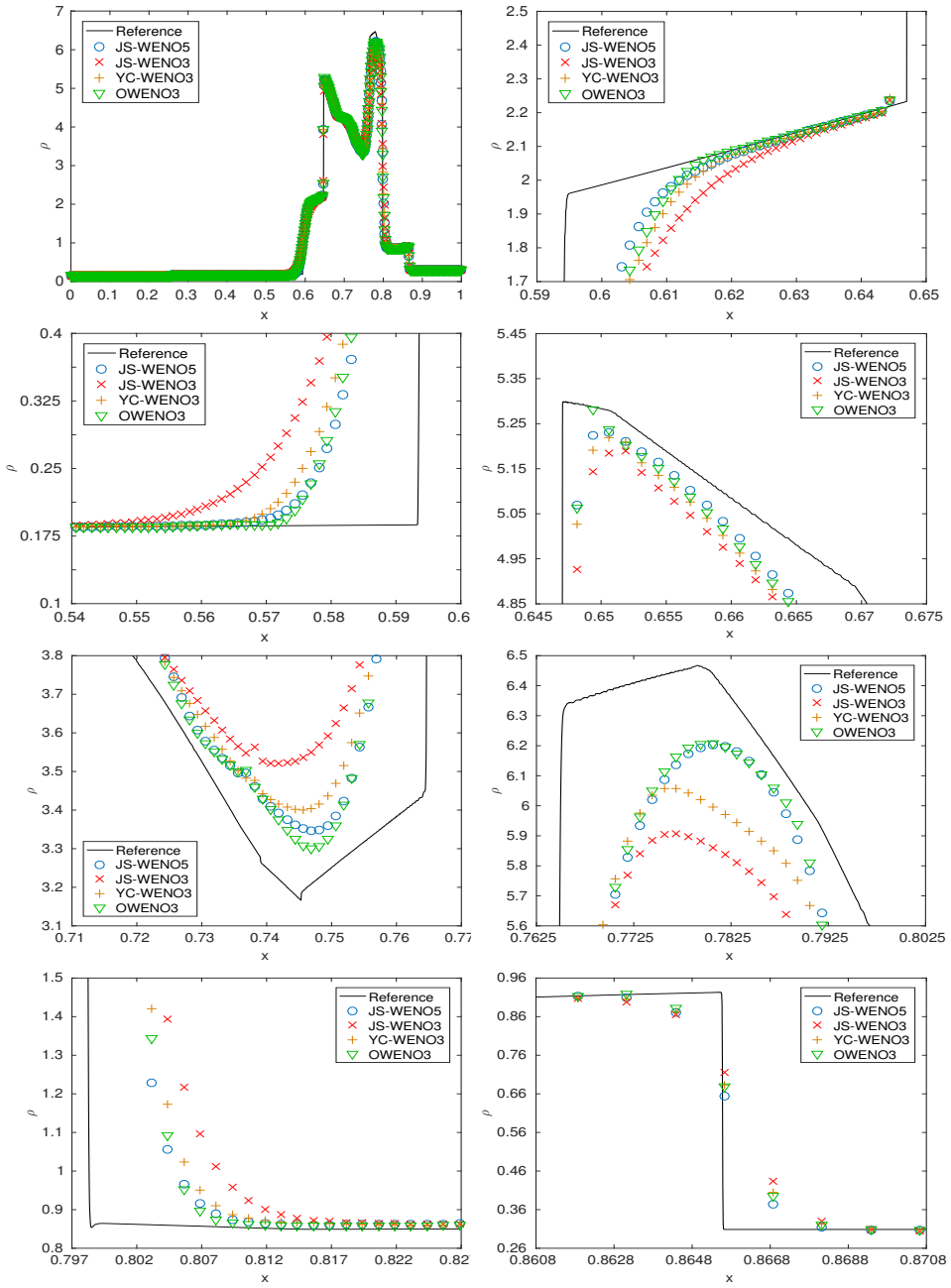

FIG. 5. *Example* 4a: *Blast wave problem.* $T = 0.038$.

$$(\rho, v^x, v^y, E)(x, y, 0) = \begin{cases} \boldsymbol{c}_1 = (\rho_1, v_1^x, v_1^y, E_1) & \text{if } y \le \frac{1}{4} + \tan(\frac{\pi}{6})x, \\ \boldsymbol{c}_2 = (\rho_2, v_2^x, v_2^y, E_2) & \text{if } \frac{1}{4} + \tan(\frac{\pi}{6})x, \end{cases}$$

$$\boldsymbol{c}_1 = \big(8, 8.25\cos(\pi/6), -8.25\sin(\pi/6), 563.5\big), \quad \boldsymbol{c}_2 = (1.4, 0, 0, 2.5).$$

We impose inflow boundary conditions, with value $\boldsymbol{c}_1$, at the left side, $\{0\} \times [0, 1]$, outflow boundary conditions both at $[0, \frac{1}{4}] \times \{0\}$ and $\{4\} \times [0, 1]$, reflecting boundary

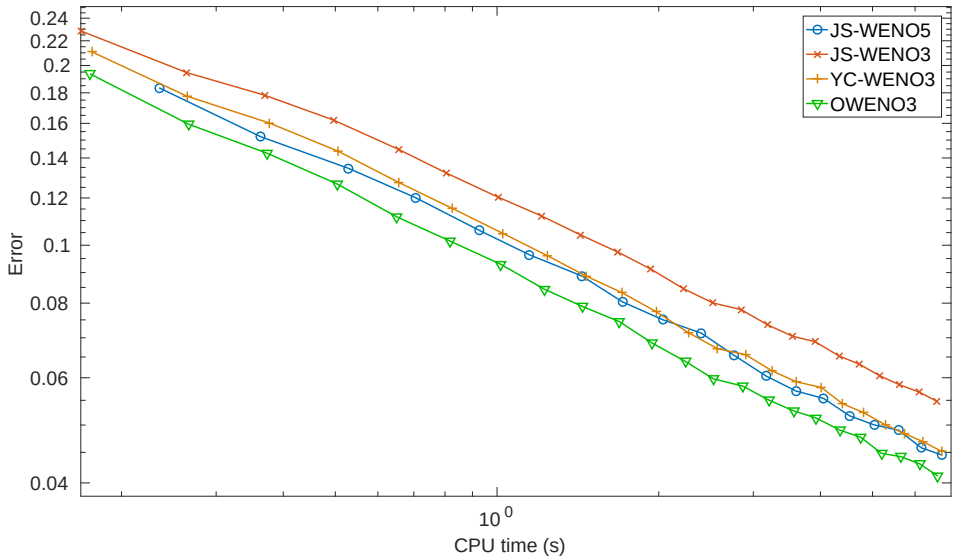

FIG. 6. *Example* 4b: *Ratio error/CPU comparison for blast wave problem.*

conditions at $]\frac{1}{4}, 4] \times \{0\}$ and inflow boundary conditions at the upper side, $[0, 4] \times \{1\}$, which mimics the shock at its actual traveling speed:

$$(\rho, v^x, v^y, E)(x, 1, t) = \begin{cases} \boldsymbol{c}_1 & \text{if } x \leq \frac{1}{4} + \frac{1+20t}{\sqrt{3}}, \\ \boldsymbol{c}_2 & \text{if } x > \frac{1}{4} + \frac{1+20t}{\sqrt{3}}. \end{cases}$$

We run different simulations until $T = 0.2$ at a resolution of 2560×640 points, shown in Figure 7, with CFL $= 0.4$ and involving the classical JS-WENO5 scheme and the third-order schemes considered along this paper.

In this case, we can see that in both resolutions, both the YC-WENO3 scheme and the OWENO3 scheme have a higher resolution than the JS-WENO3 scheme, in which the discontinuities and the nonsmooth features such as turbulence and vorticity are more smeared. On the other hand, the resolution shown by the former schemes is still remarkably lower than the JS-WENO5 scheme. This is probably due to the nature of this problem, which has no solution for the inviscid 2D Euler equations, since more and more turbulent structures appear at smaller levels as resolution is increased. Indeed, it is well known that the resolution obtained in this particular problem is strongly related with the number of points used for the reconstructions, so that, unlike the other problems presented herein, in this case increasing arbitrarily the order of the scheme seems to improve considerably its efficiency. Finally, in order to stress out the performance of our schemes, with the different time discretizations, at a same resolution, we show in Table 4 the computational time taken by all these combinations.

One can see that, for instance, the JS-WENO5 schemes combined with the third-order TVD Runge–Kutta time discretization [21] is almost three times slower than any of the third-order optimal WENO approaches with an approximate Lax–Wendroff time discretization.

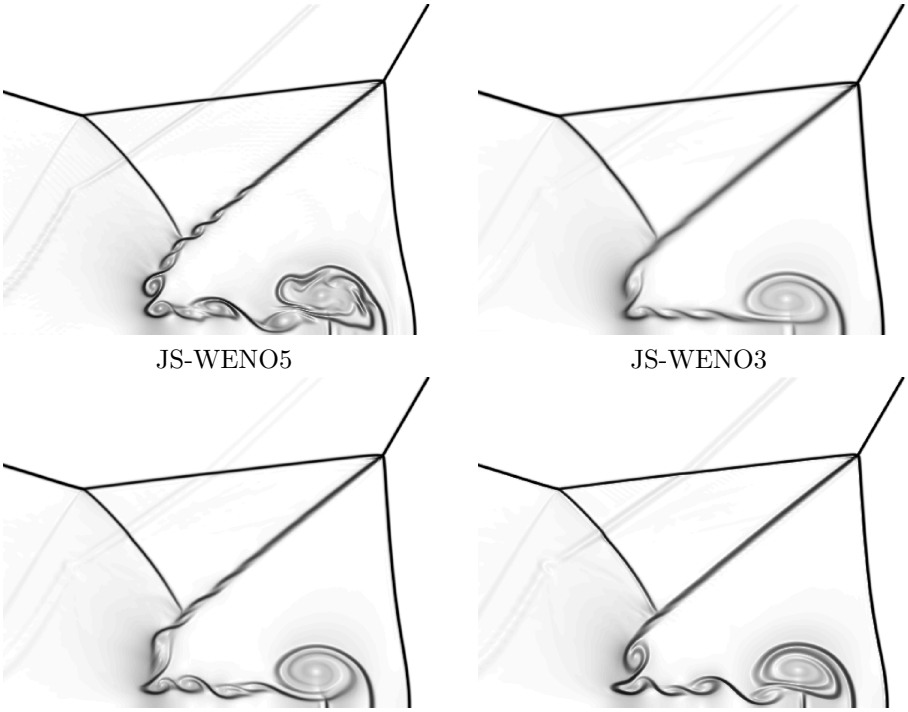

FIG. 7. *Example* 5a: *Double Mach reflection,* 2560×640. $T = 0.2$. *Schlieren plot of the density field.*

TABLE 4

Example 5b: *Computational time (seconds) with a resolution of* 256×64 *grid points.* $T = 0.2$, CFL $= 0.25$. *RK3, third-order TVD Runge–Kutta time discretization; LW, Lax–Wendroff time discretization; ALW, approximate Lax–Wendroff time discretization.*

	RK3	LW	ALW
JS-WENO5	85.76	65.63	64.53
JS-WENO3	56.56	33.72	30.46
YC-WENO3	57.04	34.42	30.82
OWENO3	58.83	35.23	31.48

Examples 6a and 6b: 2D Riemann problem. Now we solve numerically a Riemann problem for the 2D Euler equations on the domain $(0, 1) \times (0, 1)$. An early study of Riemann problems for 2D Euler equations is [19]. The initial data is taken as

$$\boldsymbol{u}(x, y, 0) = (\rho(x, y, 0), \rho(x, y, 0)v^x(x, y, 0), \rho(x, y, 0)v^y(x, y, 0), E(x, y, 0))$$

with the constants (see [13, section 3, Configuration 3])

$$\begin{pmatrix} \rho(x,y,0) \\ v^x(x,y,0) \\ v^y(x,y,0) \\ p(x,y,0) \end{pmatrix}^{\mathrm{T}} = \begin{cases} (1.5, 0, 0, 1.5) & \text{for } x > 0.5,\ y > 0.5, \\ (0.5323, 1.206, 0, 0.3) & \text{for } x \le 0.5,\ y > 0.5, \\ (0.138, 1.206, 1.206, 0.029) & \text{for } x \le 0.5,\ y \le 0.5, \\ (0.5323, 0, 1.206, 0.3) & \text{for } x > 0.5,\ y \le 0.5, \end{cases}$$

with the same equation of state as in the previous test.

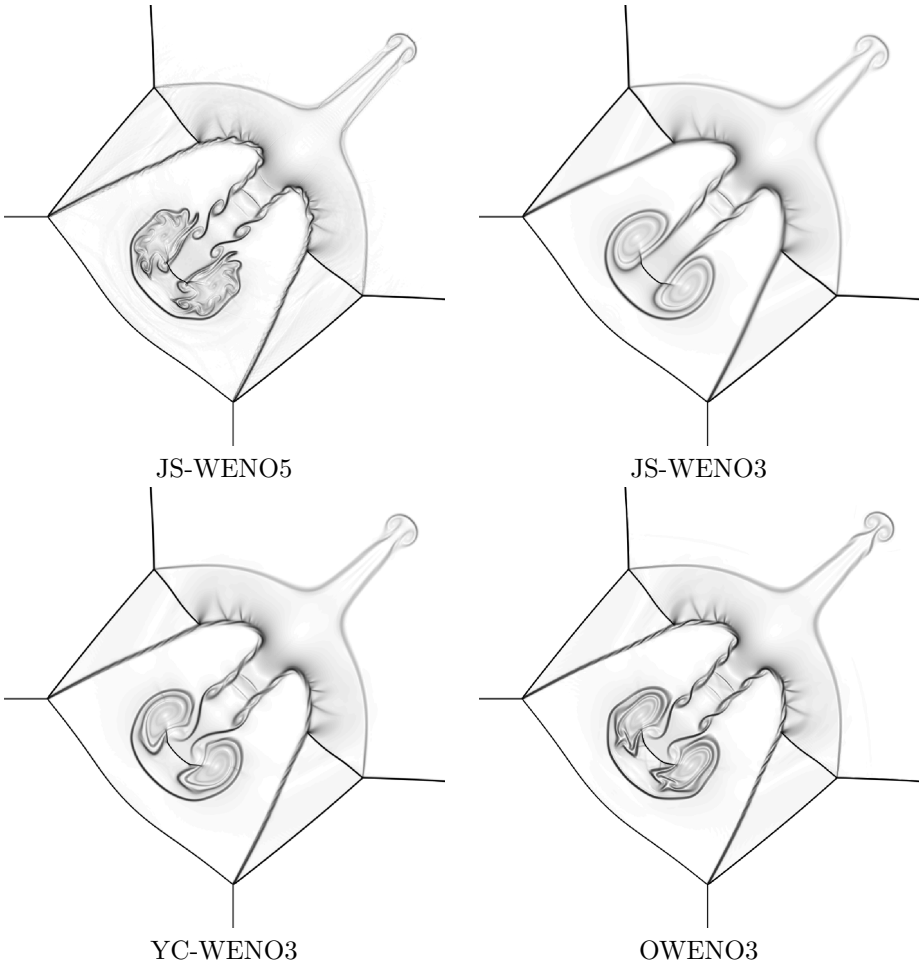

FIG. 8. *Example* 6a: *2D Riemann problem,* 2560×2560. $T = 0.3$. *Schlieren plot of the density field.*

We impose outflow boundary conditions everywhere and run this test up to time $T = 0.3$. The results can be observed in Figure 8 for a resolution of 2560×2560 points.

It can be seen that the order from lower to higher resolution is again the following one: JS-WENO3, YC-WENO3, OWENO3, and JS-WENO5, the two latter ones being close to each other. This is very significant if one takes into account that OWENO3 is faster than JS-WENO5.

With the purpose of analyzing more accurately the efficiency associated to each scheme, we now use the solutions computed with the grid of 2560×2560 points as reference solutions to perform efficiency tests by comparing error versus CPU time involving numerical solutions with grid sizes $16 \cdot 2^n \times 16 \cdot 2^n$, $n \in \{0, 1, 2, 3, 4\}$, for the involved schemes. The results are shown in Figure 9 and again indicate a higher performance for the OWENO3 scheme with respect to their third-order traditional counterparts.

Examples 7a and 7b: 2D Mach 3 wind tunnel with a step. This well-known problem involves 2D Euler equations and was proposed in [7, 22]. It consists in

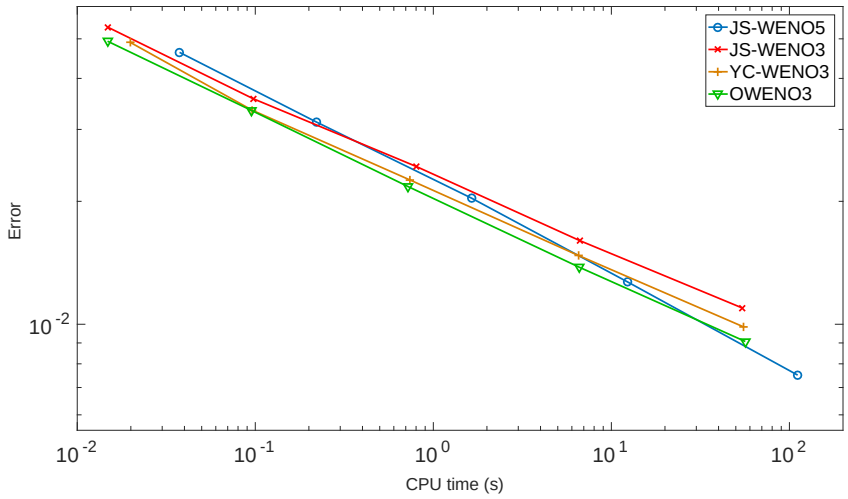

FIG. 9. *Example* 6b: *2D Riemann problem, efficiency plot.*

TABLE 5
Example 7b: *Computational time (seconds) with a resolution of* 120×40 *grid points.* $T = 4$.

	RK3	LW	ALW
JS-WENO5	69.46	55.95	54.60
JS-WENO3	52.40	27.29	26.69
YC-WENO3	52.71	27.34	27.00
OWENO3	53.37	27.65	27.24

a wind tunnel of height 1 and width 3, with a 0.2-height step located at 0.6 units from the left side. A rightgoing Mach 3 flow is considered such that the initial conditions in the whole domain are $\rho = 1.4$, $v^x = 3$, $v^y = 0$, and $p = 1$. The boundary conditions are reflecting in both the step and the upper and bottom boundaries, inflow at the left with the same values as the initial condition and outflow at the right.

We perform two experiments with grid sizes $h_x = h_y = 1/400$ and $h_x = h_y = 1/600$, computing the numerical solution using the JS-WENO5, JS-WENO3, YC-WENO3, and OWENO3 schemes until $T = 4$, which can be seen in Figures 10 and 11. A comparison regarding the CPU time involving all the schemes used for a resolution of $h_x = h_y = 1/40$ points can be also found in Table 5.

From the results, it can be seen that OWENO3 provides a sharper profile at the turbulent zone near the top of the domain while having a very similar computational cost than its classical third-order counterparts.

5. Conclusions. In this paper it has been proven that a third-order interpolator with a three-point stencil cannot simultaneously detect discontinuities and keep the optimal third-order accuracy near critical points unless a scale-dependent parameter is used. As a consequence, a third-order scheme, whose numerical flux interpolator includes a fourth additional node (used only for the computation of the weights), based on a WENO approach with unconditionally third-order optimal accuracy on smooth data and without relying on any tuning parameter, has been presented. The resulting scheme maintains the width of the domain of dependence (a stencil of at most four points is used to obtain each numerical flux, as in the traditional third-order WENO schemes), and the accuracy properties of the proposed method have been proved

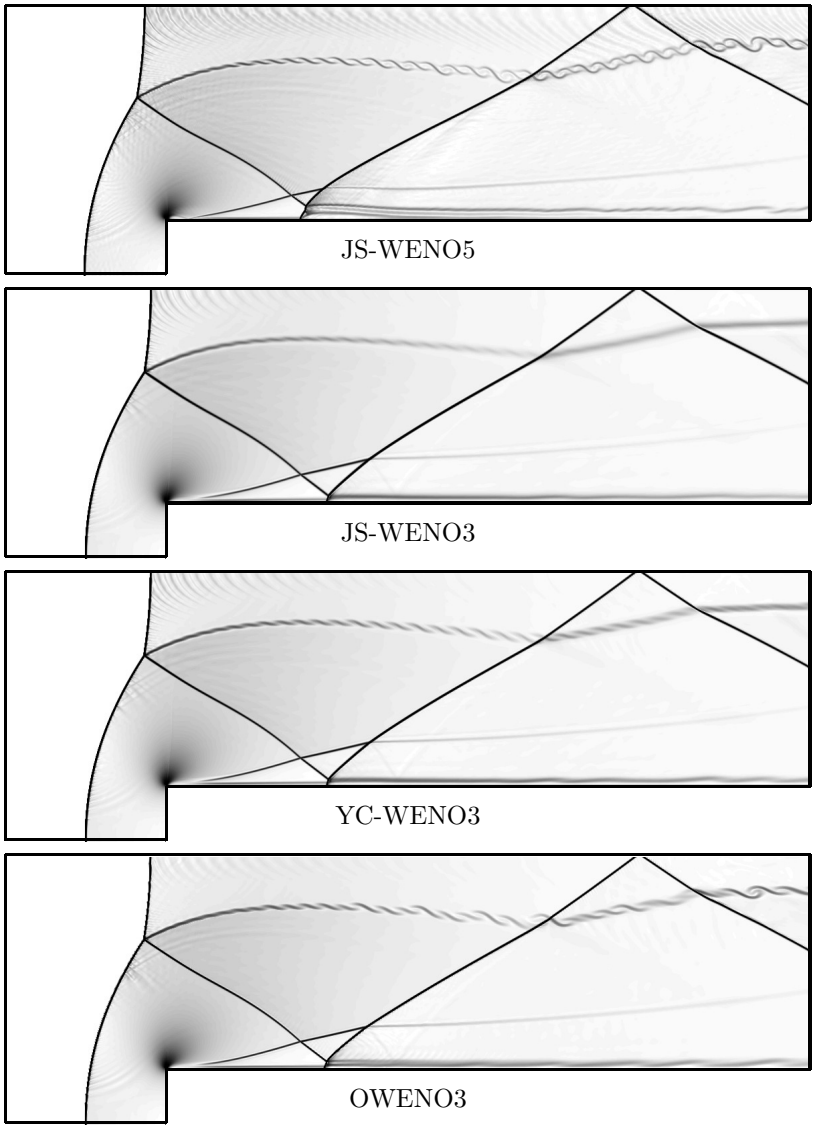

FIG. 10. *Example* 7a: 2*D Mach* 3 *wind tunnel with a step,* $h_x = h_y = 1/400$. $T = 4$. *Schlieren plot of the density field.*

theoretically and confirmed numerically along experiments involving algebraic problems and hyperbolic conservation laws. The novel scheme is more efficient than the other three-order methods considered and in most cases outperforms even the classical fifth-order JS-WENO scheme. Only in some problems involving very small-scale features, like the double Mach reflection test, is the fifth-order method competitive. However, it must be also taken into account that the third-order schemes considered in this paper allow higher values of the CFL in the aforementioned complicated problems, and therefore, even in these cases third-order schemes may be worth being used instead as well.

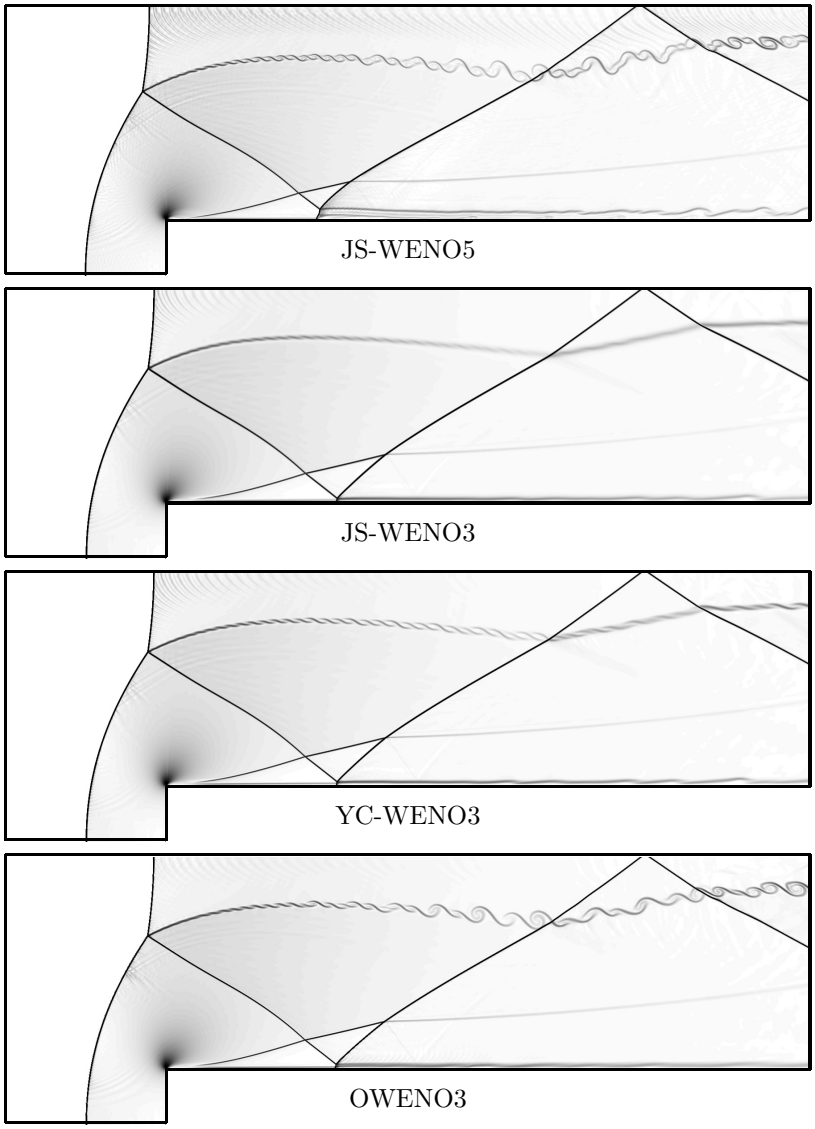

FIG. 11. *Example* 7a: 2*D Mach* 3 *wind tunnel with a step,* $h_x = h_y = 1/600$. $T = 4$. *Schlieren plot of the density field.*

REFERENCES

[1] F. ARÀNDIGA, A. BAEZA, A. M. BELDA, AND P. MULET, *Analysis of WENO schemes for full and global accuracy*, SIAM J. Numer. Anal., 49 (2011), pp. 893–915.

[2] A. BAEZA, P. MULET, AND D. ZORÍO, *The Maximal Order of Semidiscrete Schemes for Quasi-linear First Order Partial Differential Equations*, arXiv:1607.00210, 2016.

[3] A. BAEZA, R. BÜRGER, P. MULET, AND D. ZORÍO, *On the efficient computation of smoothness indicators for a class of WENO reconstructions*, J. Sci. Comput., 80 (2019), pp. 1240–1263.

[4] A. BAEZA, R. BÜRGER, P. MULET, AND D. ZORÍO, *WENO reconstructions of unconditionally optimal high order*, SIAM J. Numer. Anal., 57 (2019), pp. 2760–2784.

[5] R. Borges, M. Carmona, B. Costa, and W.S. Don, *An improved weighted essentially non-oscillatory scheme for hyperbolic conservation laws*, J. Comput. Phys., 227 (2008), pp. 3191–3211.
[6] R. Donat and A. Marquina, *Capturing shock reflections: An improved flux formula*, J. Comput. Phys., 125 (1996), pp. 42–58.
[7] A. F. Emery, *An evaluation of several differencing methods for inviscid fluid flow problems*, J. Comput. Phys., 2 (1968), pp. 306–331.
[8] N. R. Gande, Y. Rathod, and S. Rathan, *Third-order WENO scheme with a new smoothness indicator*, Internat. J. Numer. Methods Fluids, 85 (2017), pp. 90–112.
[9] N. R. Gande, Y. Rathod, and S. Rathan, *Improved third-order weighted essentially nonoscillatory scheme*, Internat. J. Numer. Methods Fluids, 87 (2018), pp. 329–342.
[10] A. K. Henrick, T. D. Aslam, and J. M. Powers, *Mapped weighted essentially non-oscillatory schemes: Achieving optimal order near critical points*, J. Comput. Phys., 207 (2005), pp. 542–567.
[11] P. Holoborodko, *MPFR C++*, http://www.holoborodko.com/pavel/mpfr/.
[12] G. S. Jiang and C.-W. Shu, *Efficient implementation of weighted ENO schemes*, J. Comput. Phys., 126 (1996), pp. 202–228.
[13] A. Kurganov and E. Tadmor, *Solution of two-dimensional Riemann problems for gas dynamics without Riemann problem solvers*, Numer. Methods Partial Differential Equations, 18 (2002), pp. 584–608.
[14] X.-D. Liu, S. Osher, and T. Chan, *Weighted essentially non-oscillatory schemes*, J. Comput. Phys., 115 (1994), pp. 200–212.
[15] *The GNU MPFR Library*, http://www.mpfr.org/.
[16] J. Qiu and C.-W. Shu, *Finite difference WENO schemes with Lax-Wendroff-type time discretizations*, J. Sci. Comput., 24 (2003), pp. 2185–2198.
[17] B. Schmidtmann, R. Abgrall, and M. Torrilhon, *On third-order limiter functions for finite volume methods*, Bull. Braz. Math. Soc. (N. S.), 47 (2016), pp. 753–764.
[18] B. Schmidtmann, R. Abgrall, and M. Torrilhon, *Relations between WENO3 and third-order limiting in finite volume methods*, J. Sci. Comput., 68 (2016), pp. 624–652.
[19] C.W. Schulz-Rinne, *Classification of the Riemann problem for two-dimensional gas dynamics*, SIAM J. Math. Anal., 24 (1993), pp. 76–88.
[20] C.-W. Shu and S. Osher, *Efficient implementation of essentially non-oscillatory shock-capturing schemes*, J. Comput. Phys., 77 (1988), pp. 439–471.
[21] C.-W. Shu and S. Osher, *Efficient implementation of essentially non-oscillatory shock-capturing schemes*, II, J. Comput. Phys., 83 (1989), pp. 32–78.
[22] P. Woodward and P. Colella, *The numerical simulation of two-dimensional fluid flow with strong shocks*, J. Comput. Phys., 54 (1984), pp. 115–173.
[23] X. Wu, J. Liang, and Y. Zhao, *A new smoothness indicator for third-order WENO scheme*, Internat. J. Numer. Methods Fluids, 81 (2017), pp. 451–459.
[24] X. Wu and Y. Zhao, *A high-resolution hybrid scheme for hyperbolic conservation laws*, Internat. J. Numer. Methods Fluids, 78 (2015), pp. 162–187.
[25] W. Xu and W. Wu, *An improved third-order weighted essentially non-oscillatory scheme achieving optimal order near critical points*, Comput. & Fluids, 162 (2018), pp. 113–125.
[26] N. K. Yamaleev and M. H. Carpenter, *Third-order energy stable WENO scheme*, J. Comput. Phys., 228 (2009), pp. 3025–3047.
[27] N .K. Yamaleev and M. H. Carpenter, *A systematic methodology to for constructing high-order energy stable WENO schemes*, J. Comput. Phys., 228 (2009), pp. 4248–4272.
[28] D. Zorío, A. Baeza, and P. Mulet, *An approximate Lax-Wendroff-type procedure for high-order accurate schemes for hyperbolic conservation laws*, J. Sci. Comput., 71 (2017), pp. 246–273.